batteries

MDPI

Article

Zeolite-Templated Carbon with Tailored Mesoporosity as a Kinetic Enhancer for Bio-Based Hard Carbon Sodium-Ion Battery Anodes

Luca Mesina [1,2,*], Claudia Paoletti [2,*], Annalisa Aurora [2], Giorgia Greco [2], Serena Gagliardi [3], Flaminia Rondino [3], Emanuele Serra [2] and Sergio Brutti [4,*]

[1] Department of Chemical Engineering Materials Environment, La Sapienza University of Rome, Via Eudossiana 18, 00184 Rome, Italy
[2] Italian National Agency for New Technologies, Energy and Sustainable Economic Development, Technologies and Devices for Electrochemical Storage (TERIN-DEC-ACEL) Technical Unit, Via Anguillarese 301, 00123 Rome, Italy; annalisa.aurora@enea.it (A.A.); giorgia.greco@enea.it (G.G.); emanuele.serra@enea.it (E.S.)
[3] Italian National Agency for New Technologies, Energy and Sustainable Economic Development, Nuclear Department—Physical Technologies and Security Division, Via Anguillarese 301, 00123 Rome, Italy; serena.gagliardi@enea.it (S.G.); flaminia.rondino@enea.it (F.R.)
[4] Department of Chemistry, Sapienza University of Rome, Piazzale A. Moro 5, 00185 Rome, Italy
* Correspondence: luca.mesina@uniroma1.it (L.M.); claudia.paoletti@enea.it (C.P.); sergio.brutti@uniroma1.it (S.B.)

Abstract

Hard carbons (HCs) are promising sodium-ion battery anodes but suffer capacity loss at high rates due to tortuous Na^+ pathways. Here, a zeolite-templated carbon (ZTC) was introduced as a conductive, mesoporous additive (10 wt%) to a hazelnut-derived hard carbon (HEZ) to improve Na^+ transport and rate performance. Structural and porosity analyses show complementary architectures: a microporous HEZ and a highly ordered ZTC with interconnected mesopores. Electrodes containing ZTC exhibit increased apparent ionic diffusion coefficients (from ~$3.5 \cdot 10^{-10}$ to ~$16 \cdot 10^{-10}$ $cm^2 \cdot s^{-1}$ Cathodic) and enhanced rate capability. Galvanostatic intermittent titration technique (GITT) analysis indicates accelerated Na^+ transport in the low-voltage plateau region, and galvanostatic cycling demonstrates a sustained plateau capacity of ~100 $mAh \cdot g^{-1}$ for the ZTC-containing electrode after 50 cycles at 50 $mA \cdot g^{-1}$ (vs. ~30 $mAh \cdot g^{-1}$ for pristine HC). Although the ZTC increases the electrode surface area and lowers initial Coulombic efficiency, the addition markedly improves high-rate storage and capacity retention. These results demonstrate that a minor fraction of templated mesoporous carbon can effectively alleviate kinetic limitations in bio-derived HC anodes for sodium-ion batteries.

Keywords: sodium-ion batteries; hard carbon; zeolite templated carbon; bio-waste; sodium diffusion; additive

Check for updates

Academic Editors: Binghui Xu and Haichao Chen

Received: 8 July 2026
Revised: 18 September 2026
Accepted: 23 September 2026
Published: 30 September 2026

Copyright: © 2026 by the authors. Licensee MDPI, Basel, Switzerland. This article is an open access article distributed under the terms and conditions of the Creative Commons Attribution (CC BY) license.

1. Introduction

Lithium-ion batteries represent a pivotal technology of the current century, serving as the primary energy storage solution for portable electronics and electromobility [1]. However, the relative scarcity of lithium resources in the Earth's crust and their uneven geographical distribution pose complex challenges to the long-term scalability of electrical energy storage systems [2,3]. Consequently, sodium-ion batteries (SIBs) have garnered significant research interest as a compelling alternative to the lithium-ion paradigm. The

primary advantage of sodium lies in its high natural abundance, approximately 1000-fold greater than that of lithium, which ensures enhanced sustainability and cost-effectiveness. Moreover, sodium is a particularly attractive candidate due to its chemical proximity to lithium in the periodic table, resulting in the smallest ionic radius among alkali metal cations after lithium itself [4,5]. Nevertheless, for SIBs to achieve the commercial viability of established lithium-based technologies, several technological hurdles must be addressed [6]. The primary constraints of sodium relate to its higher reduction potential and larger ionic radius compared to lithium (−2.71 V vs. *SHE* and 0.102 nm for Na^+ contrasted with −3.04 V vs. *SHE* and 0.076 nm for Li^+). These intrinsic properties often result in lower energy densities and more sluggish diffusion kinetics, which can hinder effective reversible intercalation within traditional electrode materials [5–7].

Hard carbons (HCs) have emerged as the leading anode materials for SIBs, demonstrating superior performance compared to ordered carbons, such as graphite, or other disordered varieties like soft carbons [8,9]. To overcome their kinetic limitations, non-structural optimization strategies such as heteroatom doping (e.g., N, P, S) and chemical surface modifications have been widely employed to adjust interlayer spacing and surface reactivity, though frequently at the expense of synthetic complexity or elevated initial capacity loss [10,11]. Concurrently, structural design strategies targeting the reduction in tortuosity have gained attention. For instance, Bhawana et al. [12] investigated HCs derived from potato peels, achieving optimal performance at a synthesis temperature of 900 °C due to a high volume of closed pores and low tortuosity facilitated by channel-like structures. Xu et al. [13] demonstrated high performance and improved initial Coulombic efficiency (ICE) using wood biomass, leveraging its natural anisotropic characteristics to create self-supporting, low-tortuosity HCs. Furthermore, Wu et al. [14] emphasized the importance of surface tortuosity, confirming that a lower surface tortuosity effectively improves both electrochemical performance and ICE.

Alongside structural design, using additives offers another effective route to enhance hard carbon electrochemical performance. The most used additives include

1. Conventional Carbon Blacks (Super P, Ketjen black), which provide excellent electronic conductivity but minimal ion-transport enhancement due to low specific surface area (SSA) and limited, disordered porosity [15].
2. Activated Carbons, which offer high SSA but suffer from poorly controlled, heterogeneous pore distributions and elevated surface-defect densities that trigger severe, irreversible electrolyte decomposition [16,17].
3. Broadly Templated Mesoporous Carbons, commonly synthesized via hard or soft-templating methods; these materials are widely explored as anodes [18–20]. However, they exhibit broad pore distributions and high tortuosity indices, rendering them suboptimal for rapid ion transport.

In this study, we investigate the effect of incorporating a mesoporous carbon called Zeolite-Templated Carbon (ZTC) as a functional additive within a bio-derived hard carbon anode from hazelnut shells (HEZ), with the primary objective of mitigating Na^+ transport limitations at the carbon particle interface during electrochemical cycling. ZTCs constitute a class of highly ordered, three-dimensional micro- and mesoporous carbons produced through the nanocasting of zeolite frameworks, characterized by uniform nanopores (<2 nm), developed microporosity (1.7 $cm^2 \cdot g^{-1}$), and very large surface areas (up to ~4000 $m^2 \cdot g^{-1}$) [21,22]. ZTCs were first synthesized in 1997 by Kyotani et al. via a hard-casting strategy using aluminosilicate zeolite templates [23]. Although ZTC materials have demonstrated success in electrical double-layer capacitor applications [24], their implementation as functional additives in alkali-metal-ion battery anodes remains limited. Recent explorations in Li-O_2 batteries conducted by Hayat et al. [25] proved that hierarchical

ZTC structures provide superior mass transport of lithium ions compared to conventional microporous carbons, with RHO-type ZTC enhancing Li^+ diffusivity by approximately 44% over non-hierarchical ZTC electrodes. In potassium-ion batteries, Romain et al. [26] showed that ordered ZTC micropores effectively accommodate larger potassium dual-ions, providing high reversible capacity and fast insertion/extraction dynamics. Additionally, Tan et al. [27] conducted a study controlling the particle size of ZTC for use as an anode in SIBs. They revealed that the ZTC with a particle size of 10 nm exhibited the highest first discharge capacity of ~2116 $mAh \cdot g^{-1}$ at a current density of 0.1 $mA \cdot g^{-1}$. At the same current density, the ZTC with a 70 nm particle size showed a better reversible capacity of 180 $mAh \cdot g^{-1}$.

Building upon these insights, incorporating ZTC into the HEZ matrix establishes a strategic design based on hierarchical pore complementarity. This approach represents the central novelty of the present work: rather than modifying the native HC precursor or altering synthesis conditions, which inevitably changes the intrinsic microstructure, we introduce a well-defined mesoporous carbon phase as a geometrically distinct additive to lower the effective ionic tortuosity of the composite electrode. This dual-phase architecture achieves performance enhancements through three primary mechanisms:

1. Geometric Precision and Tortuosity Control: The zeolite framework yields a precise pore geometry with uniform micropores and interconnected mesopores, minimizing pore-size distribution width relative to broad soft/hard-templated carbons [21,22]. Reductions in pore tortuosity by an order of magnitude have been shown to enhance ionic diffusion rates by 2–3 orders of magnitude [28].
2. Hierarchical Structural Preservation: Unlike post-synthesis activation or chemical etching routes that sacrifice capacity-bearing micropores [21,22], the ZTC additive strategy explicitly preserves the native HC micropore structure (0.9 nm, 54 $m^2 \cdot g^{-1}$ in our HEZ) responsible for high gravimetric storage in the sloping low-voltage regime, while introducing high-surface-area mesoporous pathways (5.7 nm, 773 $m^2 \cdot g^{-1}$ in ZTC) for rapid Na^+ transport without competing for the same storage sites.
3. Dual Transport Enhancement: The ordered local turbostratic structure and high conductivity of ZTC frameworks offer interconnected electronic and ionic pathways across the electrode matrix [24].

In this work, Beta-Zeolite was employed as the templating agent, as it promotes key carbonization reactions including condensation and hydrogen transfer [29], and is amenable to removal via mild acid–base leaching procedures employing 2 M NaOH and 1 M HCl [30], thereby avoiding the use of concentrated HF, enabling a safer and more scalable synthesis. To systematically assess the impact of this synthesis route, ZTC was characterized and compared with HEZ to evaluate differences in microstructure, surface morphology, and porosity. The structural and morphological characterization presented herein reveals that, while both HEZ and ZTC share a comparable local turbostratic microstructure, as evidenced by consistent X-Ray Diffraction (XRD) and Raman parameters, they exhibit markedly distinct surface morphologies and complementary porosity distributions, as highlighted by gas analysis and Small-Angle X-ray Scattering (SAXS) measurements. This complementarity is not coincidental but is the direct consequence of the templating approach, and it forms the structural basis for the synergistic behavior of the composite electrode. The electrochemical results demonstrate that the incorporation of a minor ZTC fraction (10 wt%) is sufficient to substantially enhance ionic transport pathways, rate capability, and capacity retention under demanding cycling conditions, without requiring any modification of the HC synthesis protocol. The 10% loading was selected based on established guidelines from prior hard carbon electrode formulation studies, where conductive additive concentrations in the 5–10 wt% range had been recognized as optimal for balancing electronic conductivity

with minimized inactive surface area [31]. The 10 wt% proportion ensures sufficient ZTC content to establish continuous ionic transport pathways through the electrode matrix while avoiding excessive dilution of the electrochemically active hard carbon component.

These findings are discussed in the context of established tortuosity theory and validated through complementary kinetic analysis techniques, providing a mechanistic framework that rationalizes the observed performance enhancement and supports the broader applicability of this additive strategy to other bio-derived hard carbon systems.

2. Materials and Methods

2.1. Synthesis of Hard Carbon (HEZ)

The HC utilized in this study, hereafter referred to as HEZ, was derived from hazelnut shells via a scalable two-step process depicted in Figure 1a. Initially, the bio-waste shells (obtained from BIO NOCCIOLA srl, Carbognano, Italy) were ground using a 8000 M Mixer/Mill (SPEX SamplePrep, Metuchen, NJ, USA) in a stainless-steel jar with Ø 8 nm balls for 15 min. The resulting powder was placed in an alumina boat and pyrolyzed in a tubular oven (Carbolite Gero GmbH & Co. KG, Neuhausen, Germany). Carbonization was conducted under an Ar/H_2 flux (50 mL·min^{-1}) with a heating rate of 5 °C·min^{-1} up to a peak temperature of 1100 °C, maintained for a dwell time of 2 h.

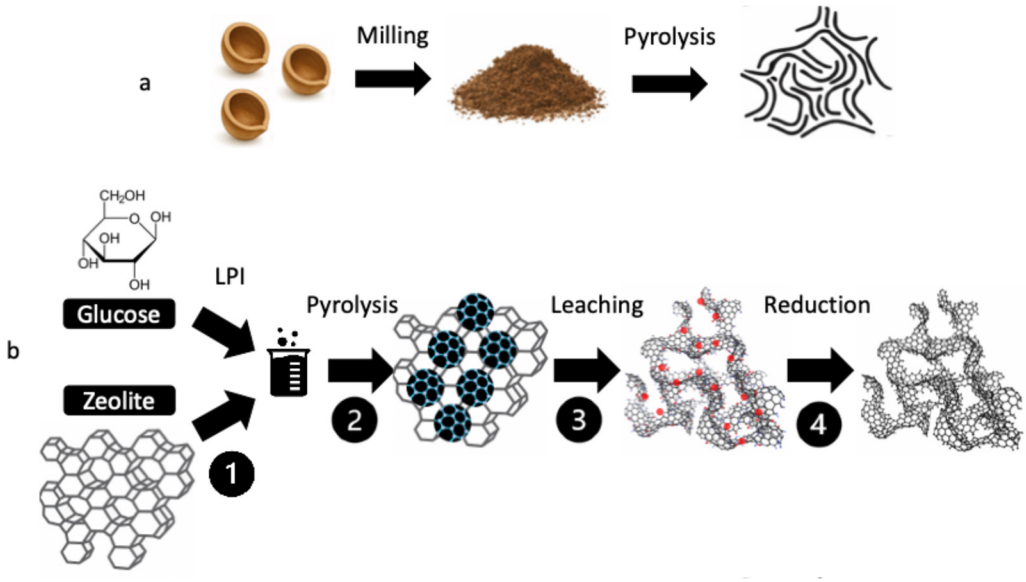


Figure 1. (**a**) HEZ synthesis: (1) milling of the hazelnut shells; (2) pyrolysis: 5 °C·min^{-1} heating rate, 1100 °C 2 h dwell time, Ar/H_2 flux 50 mL·min^{-1}. (**b**) ZTC synthesis: (1) liquid-phase impregnation (LPI): wt. ratio glucose:zeolite 1:1; (2) Pyrolysis under the same conditions as HEZ; (3) leaching: NaOH 2M at 80 °C for 2 h, HCl 1 M at RT for 2 h; (4) reduction: 5 °C·min^{-1} heating rate, 500 °C 2 h dwell time, Ar/H_2 flux 50 mL·min^{-1}.

2.2. Synthesis of Zeolite-Templated Carbon (ZTC)

The ZTC synthesis followed an original protocol adapted from the methodologies of Ruiz-Rosas et al. and Park et al. [29,31]. The process is illustrated in the flow diagram in Figure 1b. Zeolite powder (Thermo Fisher Scientific Inc., Waltham, MA, USA) was mixed with glucose (Sigma-Aldrich Chemie GmbH, Taufkirchen, Germany) in a 1:1 weight ratio and dissolved in deionized water (50 mL of water per 10 g of solid mass). The solution was stirred for 1 h at room temperature and subsequently heated to 80 °C until caramelization occurred. The resulting slurry was pyrolyzed using the same parameters as the HEZ sample (heating rate 5 °C·min^{-1}, 1100 °C 2 h dwell time, Ar/H_2 flux of 50 mL·min^{-1}). To isolate the carbon framework, the inorganic phase was removed via a two-step leaching process.

First, a desilication step was performed using a 2 M NaOH at 80 °C for 2 h in a 50% (v/v) H_2O/Ethanol mixture (40 mL per 0.5 g of material). After washing with deionized water until neutral pH, a dealumination step followed, utilizing 1 M HCl in water at RT for 2 h (100 mL per 0.5 g of material). Both steps were conducted in a round-bottom flask equipped with a reflux condenser to maintain constant concentration and temperature. The effective template removal was confirmed through XRD and Thermogravimetric Analysis (TGA) shown in Supporting Information, Section S1. As a final step, the powder was neutralized and subjected to a secondary annealing at 500 °C (5 °C·min^{-1} heating rate, 500 °C 2 h dwell time, Ar/H_2 flux 50 mL·min^{-1}) to mitigate oxygen-containing functional groups.

2.3. Material Characterization

Microstructural parameters were determined via XRD and Raman spectroscopy. XRD was performed using a SmartLab diffractometer (Rigaku Corp., Tokyo, Japan; Cu–K_α, $\lambda = 1.54$Å, 40 kV, 30 mA) over a 2θ range of 10°–80° with a step size of 0.0252° and a scan rate of 0.8°·min^{-1}. Raman spectroscopy measurements were conducted using a home-built microspectrometer, consisting of a metallographic microscope (Leica Microsystems GmbH, Wetzlar, Germany) coupled to a 550 mm monochromator (Horiba Jobin Yvon GmbH, Oberursel, Germany) equipped with a liquid-nitrogen-cooled CCD detector (Horiba Jobin Yvon GmbH, Oberursel, Germany). Excitation was provided by a 532 nm diode-pumped solid-state laser (LASOS Lasertechnik GmbH, Jena, Germany) filtered by a BraggGrate bandpass laserline filter (OptiGrate Corp., Oviedo, FL, USA) to eliminate background emission and attenuated using neutral density filters to reduce the laser power incident onto the sample to about 2 mW. The excitation was delivered to the sample through a 100X long working distance objective (Ernst Leitz Wetzlar GmbH, Wetzlar, Germany), and the resulting diffused light was collected by the same objective in a backscattering configuration and filtered by a Razor Edge longpass filter (Semrock Inc., Rochester, NY, USA) to reject the elastic component. The Raman spectra were collected using a 600 grooves/mm grating and averaging 4 measurements of 60 s each. The Raman spectra were then calibrated by comparing the experimental spectrum of a reagent-grade cyclohexane reference sample with the published one [32,33].

Surface morphology was investigated via Field Emission Scanning Electron Microscopy (FE-SEM, LEO 1530; Carl Zeiss AG, Oberkochen, Germany) utilizing the GEMINI field emission column (accelerating voltage: 200 V to 30 kV, resolution: 1 kV-3 nm at 2 mm working distance (WD), 30 kV-1 nm at 2 mm WD).

Pore size distribution and Specific Surface Area (SSA) were calculated by gas adsorption analysis: Nitrogen physisorption experiments were conducted on a TriStar II 3020 instrument (Micromeritics Instrument Corp., Norcross, GA, USA). Samples were degassed in vacuum for 4 h at 300 °C followed by overnight pumping at 120 °C before measurement. The empty volume of the cell was determined with helium.

N_2 isotherms were collected at 77 K. The SSA for each sample was determined by the Brunauer–Emmet–Teller method (BET) using data points at a relative pressure p/p° between 0.01 and 0.3. The total pore volume was determined at a relative pressure of 0.98. The pore size distribution was calculated via Tristar 2030 Plus software (v2.03), using the Barrett–Joyner–Halenda (BJH) N_2-model for slit geometry at optimal Goodness of Fit vs. Regularization (0.01) values for both root-mean-square (RMS) Error of Fit and Roughness of Distribution.

CO_2 isotherms were collected at 273.15 K. The pore size distribution was calculated via Tristar 2030 Plus software, using the density functional theory (DFT) CO_2-model for slit geometry at optimal Goodness of Fit vs. Regularization (0.01) values for both RMS Error of Fit and Roughness of Distribution.

SAXS measurements were carried out at SAXSLab Sapienza using a Xeuss 2.0 Q-Xoom instrument (Xenocs SAS, Grenoble, France). The setup was equipped with a micro-focus Genix 3D X-ray source with a Cu anode ($\lambda = 0.1542$ nm), a two-dimensional Pilatus3 R 300K detector (DECTRIS Ltd., Baden-Dättwil, Switzerland) positioned at variable sample-to-detector distances, and an additional Pilatus3 R 100K detector (DECTRIS Ltd.) placed at a fixed shorter distance from the sample, approximately 14 cm, and tilted by 36° to cover higher scattering angles. The calibration of the sample-to-detector distance was performed using silver behenate for the small-angle range and Al_2O_3 for the fixed-distance wide-angle detector. The incident beam size was set to 0.5 mm × 0.5 mm by means of a two-pinhole collimation system equipped with scatterless slits. Data were collected at two sample-to-detector distances, 262 and 2500 mm, allowing an overall explored scattering vector modulus range from q = 0.04 nm^{-1} to q = 32 nm^{-1}, where $q = 4\pi\sin\theta \cdot \lambda^{-1}$, 2θ is the scattering angle, and λ is the X-ray wavelength.

To verify the complete removal of the inorganic phase after the leaching processes, TGA was performed with a TA Instruments SDT650 system (TA Instruments, New Castle, DE, USA) under an air atmosphere (flow rate of 100 $mL \cdot min^{-1}$).

2.4. Electrochemical Measurements

Working electrodes were prepared by casting a slurry containing HEZ, binder (polyvinylidene fluoride PVDF), and carbon additives (ZTC or commercial Super P), resulting in the following three different electrode configurations:

1. HEZ 9-1 (containing HEZ:PVDF wt% 90:10);
2. HEZ_ZTC (containing HEZ:PVDF:ZTC wt% 80:10:10);
3. HEZ 8-1-1 (containing HEZ:PVDF:SuperP wt% 80:10:10).

To isolate the unique functional role of ZTC, a step-by-step control framework was established comparing an additive-free baseline (HEZ 9-1) for intrinsic hard carbon kinetics and a conventional Super P benchmark (HEZ 8-1-1) for purely electronic enhancement. Direct comparison against the target formulation (HEZ_ZTC) decouples standard electronic percolation from the dual electronic–ionic transport enabled by ZTC's interconnected 3D mesoporous network.

The mixtures were suspended in N-Methylpyrrolidone and cast onto aluminum foil using a doctor blade set at a 200 μm thickness reaching an average mass loading of active material of 3 $mg \cdot cm^{-2}$. The coated foils were dried at 60 °C under vacuum for 3 h and cut into 10 mm diameter disks. Electrodes were further dried overnight in a vacuum oven at 110 °C and transferred to an Ar-filled glove box (GP-Concept, Jacomex, Dagneux, France) for cell assembly. CR2032 coin cells were assembled in a half-cell configuration using sodium metal as the counter electrode and Whatman glass fiber separators (GF/D, Cytiva, Maidstone, UK) soaked with 100 μL of electrolyte (1 M $NaClO_4$ in anhydrous propylene carbonate).

Electrochemical performance was evaluated via galvanostatic cycling (GC), rate capability (RC), cyclic voltammetry (CV), and the galvanostatic intermittent titration technique (GITT) within a voltage window of 0.01–2.2 V. Capacity retention was assessed via GC for 50 cycles at 50 $mA \cdot g^{-1}$. RC tests were conducted by stepwise increasing of the current density every 5 cycles, using values of 10, 50, 100, and 250 $mA \cdot g^{-1}$ prior to returning to the initial 10 $mA \cdot g^{-1}$. Diffusion kinetics were investigated via CV at various scan rates (0.05, 0.1, 0.2, 0.5, 1.0, and 1.5 $mV \cdot s^{-1}$), with the apparent diffusion coefficient calculated using the Randles–Sevcik equation. For GITT, a current density of 10 $mA \cdot g^{-1}$ was applied to obtain 9 representative points at different states of charge (SoC) by maintaining potentiostatic steps at specific voltage intervals (1.2, 1.0, 0.8, 0.6, 0.4, 0.2, 0.15, 0.1, and 0.05 V) until equilibrium was reached. Equilibrium was defined by a 10-fold current decrease (to 0.1 $mA \cdot g^{-1}$), with pulse and relaxation times of 30 min and 9 h, respectively. The apparent diffusion coeffi-

cients (D_{app}) were calculated starting from CV datasets using the Randles–Sevcik equation, which assumes semi-infinite linear diffusion to a planar electrode under conditions of negligible surface reaction resistance. For porous carbon electrodes with rough morphology (as examined herein via SEM), this assumption is strictly violated; therefore, the reported D_{app} values should be interpreted as effective or apparent diffusion coefficients that integrate effects from pore geometry, Solid Electrolyte Interphase (SEI)-mediated ion transport, and electronic conductivity. Despite these caveats, the Randles–Sevcik analysis provides a consistent, comparative metric for assessing relative differences in ionic transport among the three electrode configurations, with the same methodological assumptions applied uniformly to all samples. This relative comparison is the primary utility of the CV-derived data; the derived D_{app} values should be viewed as semi-quantitative. In contrast, GITT analysis operates under quasi-equilibrium conditions and provides a more robust quantification of sodium-ion diffusivity within the solid electrode, independent of detailed pore-morphology assumptions.

The plateau capacity in the galvanostatic tests was defined as the capacity in the galvanostatic discharge profile within the voltage interval 0.01–0.1 V vs. Na^+/Na. This voltage range corresponds to the region where sodium ions fill interstitial sites in hard carbon, as widely documented in the SIB literature for HC anodes [8].

All electrochemical measurements were performed on a minimum of three independent coin cells for each electrode configuration (HEZ 9-1, HEZ 8-1-1, HEZ_ZTC) to ensure statistical reliability.

3. Results and Discussion

3.1. Material Characterization

3.1.1. Microstructure Analysis

The microstructure of hard carbon derived from hazelnut shells (HEZ) and zeolite-templated carbon (ZTC) was examined to evaluate how two distinct synthesis pathways, a scalable single-step carbonization for HEZ and a multi-step nanocasting process for ZTC, influence the resulting amorphous framework. The XRD patterns and Raman spectra are presented in Figure 2a, with the derived structural parameters summarized in Table 1.

The diffractograms and spectra shown in Figure 2 are typically associated with non-graphitizable carbon trends. Amorphous carbon diffractograms are characterized by two reflection peaks. One at around 25° (002) is due to the interlayer scattering related to stacking force, which arises from π aromatic bond sharing between parallel graphene layers. Instead, the second reflection peak observed at around 45° (10) is due to the intralayer scattering related to the in-plane layer scattering. XRD parameters were calculated using the Bragg and Scherrer equations [34]:

$$d_{002} = \frac{\lambda}{2\sin\theta_{002}}, \quad (1)$$

$$L_c = \frac{0.89\lambda}{\beta_{002}\sin\theta_{002}}, \quad (2)$$

$$L_a = \frac{1.84\lambda}{\beta_{10}\sin\theta_{10}}, \quad (3)$$

The parameters λ, β, as well as θ_{002} and θ_{10} represent the wavelength of incident X-rays, the half-peak width of the diffraction peak, and the diffraction angle, respectively. Compared to HEZ, the ZTC sample exhibits a slightly lower interplanar spacing (d_{002}) and a higher average stacking height (L_c), likely due to the structural constraints imposed by the zeolite template during carbonization. The lateral grain size (L_a) is also marginally larger for the ZTC.

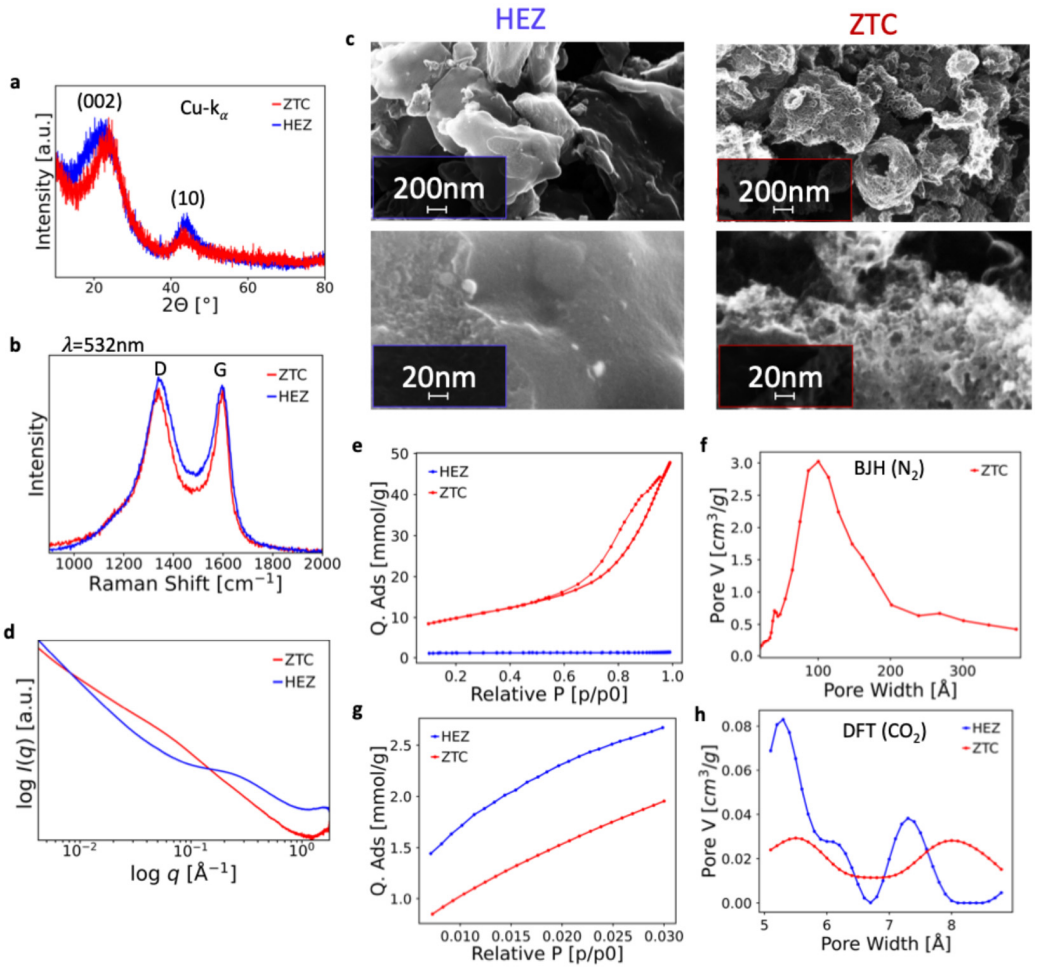


Figure 2. HEZ (blue) vs. ZTC (red): (**a**) XRD pattern; (**b**) Raman spectra; (**c**) FE-SEM images; (**d**) SAXS profile; (**e**) N_2 absorption/desorption isotherms; (**f**) BJH pore size distribution plot; (**g**) CO_2 absorption/desorption isotherms; (**h**) DFT pore size distribution plot.

Table 1. HEZ vs. ZTC structural features obtained through XRD and Raman spectroscopy. d_{002}: distances between graphene planes. L_c: stacking height. L_a: extension of graphene planes. I_D/I_G, A_D/A_G: intensity and area ratio of Raman D and G bands. SSA obtained through nitrogen sorption N_2 and SAXS.

Investigation Technique	Parameter	HEZ	ZTC
XRD	d_{002} [Å]	4.13 ± 0.01	3.90 ± 0.01
	L_c [Å]	7 ± 2	13 ± 1
	L_a [Å] *	41 ± 2	41 ± 4
Raman	I_D/I_G	1.32 ± 0.04	1.15 ± 0.02
	L_a [Å] *	18.3 ± 0.5	21.0 ± 0.4
	A_D/A_G	3.2 ± 0.2	2.9 ± 0.1
BET Specific Surface Area	SSA[$m^2 \cdot g^{-1}$] N_2	54 ± 4	773 ± 4
SAXS	Mesopore	~2.4 nm (2%)	~5.7 nm (81%)
	Micropore	~0.9 nm (98%)	~1.3 nm (19%)

* L_a value depends on the characterization technique used: XRD estimates the total lateral extension of the graphene plane (crystallite size), whereas Raman spectroscopy estimates the average distance between defects.

The Raman spectra of NGC (Figure 2b) are characterized by the presence of two broad bands centered at ~1350 cm^{-1} (D band) and ~1580 cm^{-1} (G band), respectively, attributed to defect-activated sp^2 breathing mode in rings (A_{1g}) and the C–C in-plane stretching mode (E_{2g}) [35]. For strongly disordered carbon samples, the structural parameter L_a can be obtained from the Raman spectra analysis following the methodology proposed by Ferrari et al. [36], using the following formula:

$$L_a = \sqrt{\frac{I_D}{I_G}\frac{1}{C(\lambda_L)}}, \quad (4)$$

where I_D and I_G are the heights of the peaks and $C(\lambda_L)C_0 + \lambda_L C_1$ with $C_0 = -12.6$ nm, $C_1 = 0.033$, and λ_L = laser wavelength (valid for 400 nm $< \lambda_L <$ 700 nm). To accurately account for structural defects and amorphous contributions, the I_D/I_G ratio was determined via a multi-peak fitting procedure. Specifically, a five-band decomposition method was adopted for the deconvolution of the Raman spectra [37], wherein the D, G, D1, and D4 bands were modeled using Lorentzian lineshapes, while the D3 band was fitted with a Gaussian function (Figure S2). The conventional I_D/I_G ratio was retained for calculating the Raman-derived L_a according to the Ferrari–Robertson relationship, while the integrated-area ratio A_D/A_G was additionally determined as a complementary descriptor of the relative contributions of the D and G bands. The resulting parameters are reported in Table 1, and the complete fitting parameters are provided in the Supporting Information. HEZ exhibits an I_D/I_G ratio of 1.32 ± 0.04, whereas ZTC shows a lower value of 1.15 ± 0.02, corresponding to Raman-derived L_a values of 18.3 ± 0.5 and 21.0 ± 0.4 Å, respectively. The resulting I_D/I_G ratios and the calculated L_a values demonstrate that both samples possess a comparable degree of local structural disorder.

Overall, the data suggest that both carbons share a nearly identical local microstructure, consistent with traditional hard carbon frameworks in both spectral profile and calculated parameters. This result indicates that the final nanoscale architecture is primarily governed by the pyrolysis conditions: temperature, dwell time, and atmosphere.

3.1.2. Surface Morphology, Surface Area, and Porosity Characterization

The morphology and porosity of HEZ and ZTC were compared to evaluate the impact of the templating process on the carbon structure.

Surface morphology investigated via FE-SEM revealed a profound difference in particle characteristics, as evident in Figure 2c. The HEZ sample exhibits a smooth, non-porous surface typical of biomass-derived HCs. In contrast, the ZTC displays a highly rugose and porous surface, consistent with nanocasting synthesis. Notably, a channel-like architecture can be observed in the ZTC at both magnification scales. These images qualitatively support the presence of a more open porous morphology in ZTC; however, specific pore dimensions were quantitatively assessed on the basis of N_2, CO_2 adsorption and SAXS measurements.

The specific surface area (SSA) was estimated using the BET model based on N_2 adsorption–desorption isotherms at 77 K (see Figure 2e). The ZTC isotherm displays a type IV characteristic, featuring a hysteresis loop at $p/p^\circ < 0.4$ that is commonly associated with capillary condensation phenomena typical of mesoporous carbons [38]. Consequently, the BET calculation for ZTC revealed a high SSA of 773 ± 4 $m^2 \cdot g^{-1}$, confirming a successful templating process that generated a widespread porous network accessible to N_2 molecules. Regarding the HEZ sample, the obtained results cannot be considered fully valid, as is often expected for strictly microporous materials [38,39]. Specifically, the Rouquerol plot yielded a negative C-constant, indicating that the calculated SSA does not reflect the true porosity but rather an artifact arising from the restricted accessibility of N_2 within that specific micropore range. Nevertheless, HEZ yielded a formal SSA of 54 ± 4 $m^2 \cdot g^{-1}$, which aligns

with literature values for bio-based HCs [40]. Notably, a prominent distinction lies in the N_2 adsorption capacity of the two samples, which is considerably lower for HEZ. Furthermore, the ZTC isotherm was utilized to determine the pore size distribution via the BJH method. The results highlight a substantial mesopore volume, with a size distribution centered at approximately 11 nm, alongside a small secondary distribution at 4 nm. Additionally, a complementary porosity evaluation was performed using CO_2 as a probe gas. Since CO_2 molecules are smaller and possess higher kinetic energy at 273 K, they penetrate micropores more effectively, providing a more accurate estimation of narrow porosity. The resulting isotherms show higher gas adsorption for HEZ compared to ZTC, suggesting a higher concentration of micropores in the former. Density Functional Theory (DFT) calculations were performed to quantify the micropore volume and distribution. The HEZ sample exhibits a high density of micropores with a size distribution peaking at approximately 5Å, with a minor contribution at 7Å. In contrast, ZTC presents a comparable size distribution of micropores centered at approximately 5.5Å and 8Å.

A deeper analysis of the pore distribution was conducted using SAXS. The scattering patterns for HEZ and ZTC exhibit complementary trends, reflecting distinct pore size regimes, as shown in Figure 2. The SAXS profiles were first normalized and corrected to account for the fluctuation background term (as described in the Supporting Information) [41,42]. Finally, the experimental data were fitted using the parametrization method introduced by Smarsly et al. [43] (Figure S3), which correlates the total scattered SAXS intensity I_p due to a two-phase matrix as a function of the scattering vector s, with the following parametrization model:

$$I_P(s) = \sum_{j=0}^{N} a_j I_j(2\pi bs), \quad (5)$$

The parametrization method models the experimental scattering profile as a linear combination of N analytical basis functions $I_j(s)$ which correspond to exact, mathematically defined chord length distributions $g_j(r)$ in real space. The optimization algorithm adjusts two key parameters: (i) the global length scale b, which dictates the structural size-scaling and exponential decay of the pore space, and (ii) the individual linear coefficients a_j, which represent the relative volume contribution of each discrete structural configuration j to the total porous matrix. The best fit of the experimental data determines the parameter values, enabling the quantification of the porosity range and distribution as reported in Table 1. The HEZ sample is dominated by micropores (~0.9 nm), whereas ZTC contains a significant fraction of mesopores (~5.7 nm). Specifically, the mesopore content is substantially higher in ZTC (~81%) compared to HEZ, which lacks a significant mesopore fraction (comprising only ~2% in the ~2.4 nm range). While ZTC retains a micropore volume fraction of ~19%, these pores are larger on average (~1.3 nm) than those observed in HEZ. In contrast to surface-related techniques such as gas adsorption and SEM, SAXS analysis reveals a smaller size range for both micro- and mesoporosity. This is expected, as the high penetration power of X-rays inherently provides information regarding bulk porosity.

Taken together, SEM, gas analysis, and SAXS characterizations consistently show that ZTC supplies an interconnected mesoporous network that complements the intrinsic microporosity of HEZ.

3.2. Electrochemical Measurements

3.2.1. Galvanostatic Cycling and Rate Capability Tests

The electrochemical performance was evaluated by testing the three distinct electrode configurations HEZ 9-1, HEZ_ZTC, and HEZ 8-1-1 described above. All the electrochemical results are illustrated in Figures 3 and S4. The specific capacity values reported throughout

this work are explicitly calculated based on the total active carbonaceous material mass (comprising both the HEZ hard carbon host and the carbon additives, ZTC or Super P), which represents 90 wt% of the total dry electrode layer. The 10 wt% PVDF binder is electrochemically inactive and was excluded from all specific capacity normalizations.

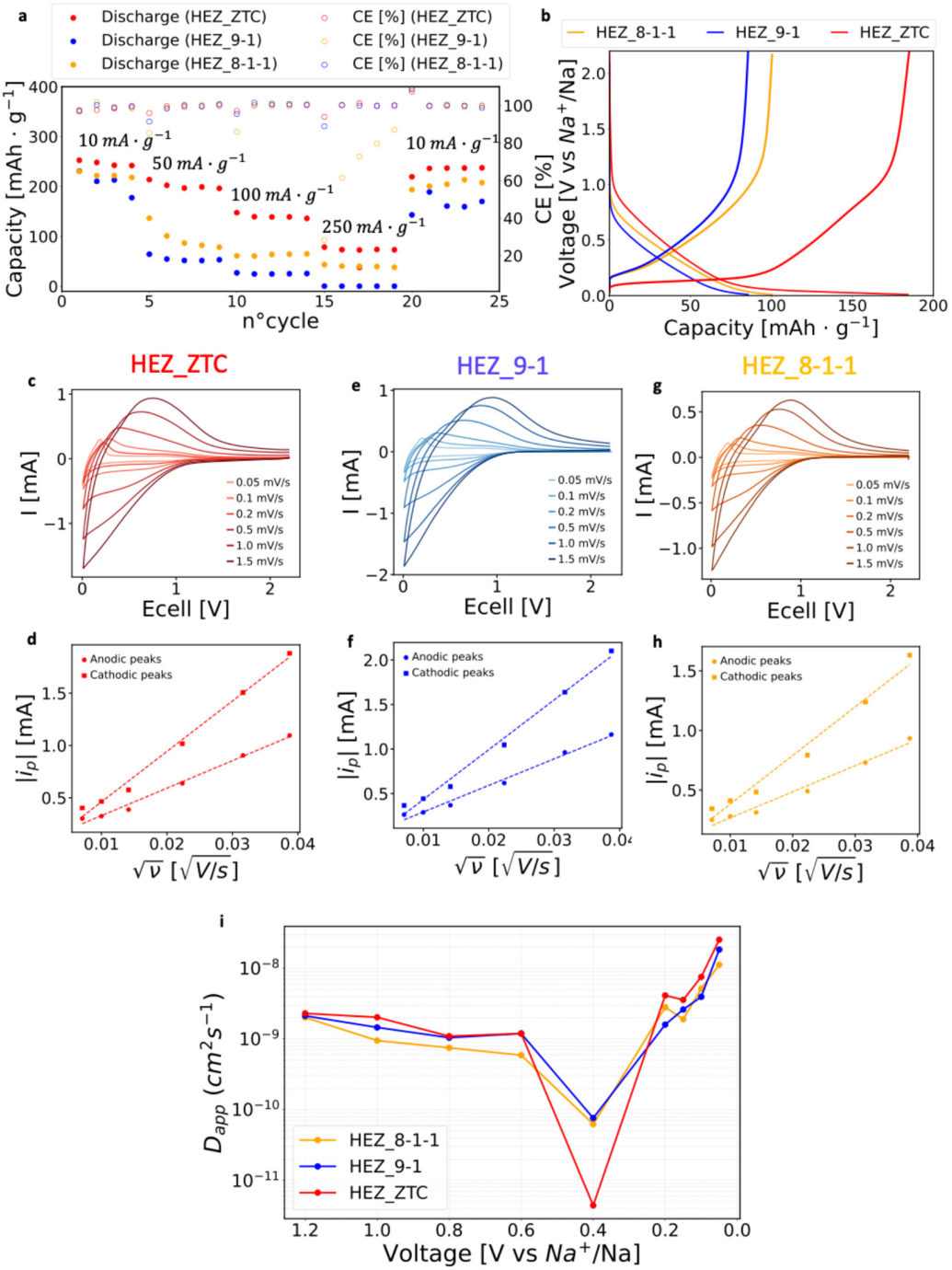


Figure 3. Electrochemical measurements of HEZ 9-1, HEZ 8-1-1, and HEZ_ZTC: (**a**) Rate capability tests performed for 5 cycles at various current densities (10, 50, 100, 250 mA·g^{-1} and again 10 mA·g^{-1}) starting from the 2° cycle; (**b**) comparison of the V vs. Q profiles at the 50th cycle (50 mA·g^{-1}); (**c**–**h**) CV obtained by varying the scan rate and the current peak vs. squared scan rate (Ip vs.$\sqrt{v}$) to obtain the apparent diffusion coefficient through the Randles–Sevcik equation; (**i**) apparent sodium-ion diffusion coefficients (D_{app}) calculated through Equation (6) for the three electrode configurations. Values represent the mean capacities and D_{app} derived from three independent cell measurements.

The initial cycle, which is critical for the formation of the SEI, is detailed in Figure S4. HEZ_ZTC electrode exhibited higher first-cycle irreversibility compared to the other samples. This resulted in a lower ICE of 53%, compared to 73% for HEZ 9-1 and 84% for HEZ 8-1-1.

The lower initial Coulombic efficiency ICE of the HEZ_ZTC electrode is likely caused by the additive's large specific surface area (773 $m^2 \cdot g^{-1}$, Table 1) [44]. As shown in the first-cycle CV profiles (Figure S4b), this high surface area promotes irreversible electrochemical reactions in the low-potential region (~0.5 V vs. Na^+/Na). Sodiation on the ZTC surface consumes active sodium ions and leads to the deposition of organic–inorganic species on the electrical double layer, increasing the amount of irreversible capacity lost. Differences in the first-cycle discharge profiles (Figure S4a) highlight distinct sodiation kinetics driven by the unique surface properties and porosity of each additive. Specifically, non-porous Super P particles and highly porous ZTC form different electrolyte–electrode interface interactions, leading to slight variations in equilibrium potentials during the initial reduction.

Despite the different ICE, the specific capacity stabilized at approximately 250 $mAh \cdot g^{-1}$ for all electrodes during subsequent cycles at a low current density of 10 $mA \cdot g^{-1}$ (Figure 3a). However, at higher current densities, the performance benefits of the ZTC additive became evident. As shown in the rate capability plot (Figure 3a and Table S3), the HEZ_ZTC electrode maintained significantly higher capacities across all investigated current densities. This enhancement was most pronounced at 50 $mA \cdot g^{-1}$ and 100 $mAh \cdot g^{-1}$. Furthermore, the stable trend in Coulombic efficiency of the ZTC-containing electrode indicates improved cycling stability.

An additional feature of the rate-capability experiment is the lower and progressively increasing Coulombic efficiency observed for HEZ_8-1-1, the electrode containing 10 wt% Super P at a current density of 250 $mA \cdot g^{-1}$. This behavior differs from the initial Coulombic inefficiency associated with SEI formation and is observed during the subsequent rate-dependent cycling sequence. At elevated current densities, polarization in Na||HC half-cells can become significant and may limit the extent of sodiation/desodiation reached within the imposed potential window. Therefore, the transient reduction in Coulombic efficiency observed for HEZ_8-1-1 may arise from a combination of current-dependent polarization and interfacial processes associated with the Super P-containing composite.

The impact of the ZTC additive is further highlighted by analyzing the voltage profiles at a constant current density of 50 $mA \cdot g^{-1}$ (Figure 3b). After 50 cycles, the HEZ_ZTC electrode maintained a plateau capacity of ~100 $mAh \cdot g^{-1}$ (capacity between the 0.01–0.1 V range) after 50 cycles at 50 $mA \cdot g^{-1}$, whereas HEZ 9-1 and HEZ 8-1-1 declined to only ~30 $mAh \cdot g^{-1}$. Beyond the 50 cycle milestone, extended testing reveals a ~30% capacity decay between the 50th and 100th cycles for HEZ_ZTC. Translating these capacity gains into practical long-term battery deployment (>500–1000 cycles) will require interphase optimization such as transitioning to more stable electrolyte systems (e.g., 1 M $NaPF_6$ in diglyme or EC/DEC blends) [45,46], incorporating film-forming additives (e.g., FEC, DFEC) [47], or tuning ZTC loading (~5 wt%) to balance rate kinetics with long-term passivation.

These results suggest that the ZTC framework enhances the electrode's ability to store Na^+ ions at higher current densities while maintaining performance at lower rates.

Overall, the increased first-cycle irreversibility of HEZ_ZTC parallels the high surface area of the ZTC component and reflects enhanced electrochemical accessibility of the ZTC pores; the same feature enables superior ionic transport at elevated current densities. While this represents an apparent penalty, two factors mitigate its impact: (1) ICE recovers to >99% rapidly by cycle 4 because the SEI layer, once formed, provides a protective barrier against further electrolyte decomposition; and (2) the low-voltage plateau capacity retention

improvements at high rates are around three times higher compared with pristine HC, far exceeding the magnitude of the first-cycle loss across longer cycling regimes.

The performance gains demonstrated by HEZ_ZTC electrodes must also be discussed against potential volumetric penalties. ZTC materials exhibit lower tap density (d ~ 0.5 g·cm^3) compared to densified hard carbon (d ~ 1.0–1.1 g·cm^3), reflecting their high porosity. When incorporated as a 10 wt% additive, this results in a modest (~8–12 wt%) reduction in the electrode volumetric tap density. For a half-cell operating at 50 mA·g^{-1} for 50 cycles, the HEZ_ZTC electrode achieves a volumetric capacity of ~50 Wh·L^{-1}, (based on plateau capacity of 100 mAh·g^{-1} and average discharge voltage of 0.5 V, normalized to electrode volume). While this is lower than densified pure-HC electrodes (~60 Wh·L^{-1}), the factor becomes economically favorable in fast-charging scenarios (>100 mA·g^{-1}), where pure HC suffers catastrophic capacity loss, and HEZ_ZTC maintains >80% of its plateau capacity. For stationary energy storage systems prioritizing power density over volumetric energy, the ZTC-additive strategy offers distinct advantages.

3.2.2. Na^+ Diffusion Analysis

To elucidate the mechanism behind the rate capability enhancement, CV and GITT analysis were conducted. To correctly interpret the kinetic parameters, it is essential to define the physical meaning of the diffusion coefficients derived from electrochemical techniques in porous composite electrodes. The D_{app} values calculated from both CV (Randles–Sevcik model) and GITT (Weppner–Huggins model) represent effective or apparent diffusion coefficients. Rather than isolating intrinsic solid-state diffusion within the hard carbon lattice, these parameters reflect a coupled transport process operating across the composite electrode matrix. This integrated process encompasses: (i) liquid-phase Na^+ transport within the electrolyte-filled macro-, meso-, and open micropore networks; (ii) interfacial charge transfer and ion migration across the SEI; and (iii) solid-state insertion/diffusion within the turbostratic graphitic domains and closed micropores of the HEZ host.

CV analysis was performed at various scan rates (0.05 to 1.5 mV·s^{-1}), as shown in Figure 3c–h. The apparent diffusion coefficient (D_{app}) was calculated using the Randles–Sevcik equation [48,49], which defines the linear relationship between the peak current I_p (V) and the square root of the scan rate v (V·s^{-1}):

$$I_p = K \cdot n^{3/2} \cdot A \cdot C \cdot v^{1/2} \cdot {D_{app}}^{1/2} \quad (6)$$

where K is a constant related to the electrochemical system and experimental conditions, n is the number of electrons transferred (n = 1 for Na^+), A is the electrode surface area (cm^2), C the bulk concentration of the electroactive species (mol·cm^{-3}) and D_{app} the apparent diffusion coefficient (cm^2·s^{-1}). This equation was applied to evaluate diffusion during both the reduction (sodiation) and oxidation (desodiation) processes.

The D_{app} values summarized in Table 2 confirm that the Super P and ZTC additives effectively accelerate Na^+ transport. Both the cathodic and anodic Na^+ diffusion coefficients improve progressively from the HEZ 9-1 to HEZ 8-1-1 and HEZ_ZTC samples, with the highest diffusion observed in the electrode containing ZTC.

To further investigate the increased plateau capacity, the galvanostatic intermittent titration technique (GITT) was employed [50]. This technique allows for the determination of D_{app} at different SoC by analyzing potential relaxation after a current pulse. According to Fick's second law, D_{app} can be derived from the following relationship:

$$D_{app} = \frac{4}{\pi\tau}\left(\frac{m_B V_M}{M_B A}\right)^2 \left(\frac{\Delta E_s}{\Delta E_\tau}\right)^2, \quad (7)$$

Table 2. D_{app} calculated through Equation (6) for the three different electrode mixtures.

Sample	Cathodic Na^+ D_{app} [$cm^2 \cdot s^{-1}$]·10^{-10}	Anodic Na^+ D_{app} [$cm^2 \cdot s^{-1}$]·10^{-10}
HEZ_ZTC	16 ± 3	2.5 ± 0.4
HEZ_8-1-1	15 ± 2	2.9 ± 0.4
HEZ_9-1	3.5 ± 0.6	1.0 ± 0.1

In this equation τ stands for the pulse duration, m_B refers to the mass of active material on the electrode, A denotes the electrode area, M_B and V_M are, respectively, the molecular weight and molar volume of the sample, ΔE_s is the steady-state voltage change, and ΔE_τ is the total voltage change during the current pulse. GITT measurements reveal a pronounced dependence of the apparent diffusion coefficient on potential (Figure 3i and Table S2), pointing to SoC-dependent transport kinetics. All three electrode configurations show a marked minimum around 0.4 V, followed by a recovery of D_{app} at lower potentials. The apparent diffusivity reflects the combined effects of electrolyte transport, interfacial/SEI transport, and Na^+ storage within the hard-carbon structure. The minimum around 0.4 V is consequently interpreted as a kinetic bottleneck within the sloping region rather than as evidence of a discrete phase transition; this is attributed to the change from the intercalation to pore-filling process [44]. At lower potentials, the recovery of D_{app} is consistent with the change in the dominant Na-storage mechanism approaching the low-voltage plateau. Across the entire potential range, the ZTC-containing electrode consistently exhibits superior D_{app} values at both high and low voltages, most notably in the low-voltage region where the primary sodium-storage process occurs while simultaneously showing the deepest D_{app} drop at 0.4 V.

The apparent diffusion coefficients derived from CV analysis (Randles–Sevcik method) show clear enhancement upon ZTC incorporation (Table 2). Cathodic D_{app} values increase from 3.5 ± 0.6·10^{-10} $cm^2 \cdot s^{-1}$ (HEZ 9-1) to 16 ± 3·10^{-10} $cm^2 \cdot s^{-1}$ (HEZ_ZTC), representing an acceleration of sodium uptake kinetics. While these values should be considered apparent coefficients due to the rough, porous electrode morphology, the consistent application of the Randles–Sevcik methodology to all samples provides valid relative comparisons. The GITT-derived D_{app} values (Figure 3d) provide orthogonal confirmation of enhanced diffusion in the low-voltage plateau region (<0.1 V), where GITT analysis is less sensitive to morphological factors and surface resistance variations.

3.2.3. Future Prospective

To contextualize the hazelnut shell hard carbon/zeolite-templated carbon (HEZ_ZTC) composite anode within contemporary carbon architectures and advanced energy storage systems, Table 3 contrasts our hierarchical mesoporous additive strategy against recent biomass-derived hard carbons [12,51–55].

As detailed in Table 3, contemporary biomass-derived hard carbon architectures rely on a diverse spectrum of precursor sources, including agricultural waste, peels, and shells, and processing strategies ranging from direct carbonization to chemical activation and acid digestion. Across these systems, specific reversible capacities generally fall between 210 and 300 mAh·g^{-1} under varying current densities (10–50 mA·g^{-1}), accompanied by ICE ranging from modest (32–55%) to relatively high values (up to 77%).

In comparison, the composite HEZ_ZTC electrode delivers a competitive initial reversible capacity of 250 mAh·g^{-1} at 10 mA·g^{-1} while maintaining an outstanding low-voltage plateau capacity retention of 100 mAh·g^{-1} at 50 mA·g^{-1} after 50 cycles. The primary trade-off of the ZTC-assisted strategy is a lower initial Coulombic efficiency. How-

ever, the rapid interfacial stabilization occurs, enabling superior long-term plateau capacity retention under high-rate conditions.

Table 3. Comparison of synthesis conditions, testing parameters, specific reversible capacities, and ICE of the hazelnut shell-derived hard carbon (HEZ_ZTC) synthesized in this work against other reported biomass-derived carbon materials.

Active Material	Synthesis Conditions	Current Density	Specific Reversible Capacity (Plateau Capacity)	ICE (%)	Reference
Hazelnut Shell HC_ZTC (HEZ_ZTC)	Direct pyrolysis at 1100 °C (2 h, Ar/H_2 flux); + ZTC additive	10 mA·g^{-1}	250 mAh·g^{-1}	53%	This Work
Palm Fiber Waste	Chemical activation (KOH/H_3PO_4), pyrolysis at 800 °C (2 h, N_2 flux)	50 mA·g^{-1}	280 mAh·g^{-1}	75%	Al-Aoh et al. (2026) [51]
Apple Pomace	Pectin extraction, pyrolysis at 1100 °C (2 h, Ar flux)	50 mA·g^{-1}	285 mAh·g^{-1}	66%	Dou et al. (2018) [52]
Potato Peel	Washing, drying, pyrolysis at 900 °C (1 h, Ar flux)	35 mA·g^{-1}	300 mAh·g^{-1}	62%	Bhawana et al. (2023) [12]
Coffee Grounds, Sunflower Seed Shells, and Rose Stems	Hydrothermal carbonization, followed by pyrolysis at 1200 °C (2 h, N_2flux)	25 mA·g^{-1}	210–280 mAh·g^{-1}	32–76%	Nieto et al. (2023) [53]
Macadamia Nutshells	Direct pyrolysis at 1100 °C (1 h, N_2 flux)	20 mA·g^{-1}	210 mAh·g^{-1}	63%	Wang et al. (2025) [54]
Wild Giant Cane, Olive Stone, and Hazelnut Shells	Hydrothermal carbonization, followed by pyrolysis at 1100 °C (2 h, Ar/H_2 flux)	10 mA·g^{-1}	220–290 mAh·g^{-1}	55–77%	Ficca et al. (2026) [55]

Beyond bio-carbon anode comparisons, the kinetic design principles implemented in this work closely parallel recent advances across complementary electrochemical storage systems. For instance, Azemtsop Manfo et al. [56] demonstrated that integrating asymmetric ionic liquid cations into polyvinyl alcohol/sodium thiocyanate (PVA/NaSCN) polymer electrolytes modulates the matrix free volume and lowers ion-pairing resistance, significantly boosting ionic transport. Analogously, introducing ZTC into the HEZ active layer establishes continuous, low-resistance mesoporous highways that alleviate local concentration polarization during rapid Na^+ delivery. Furthermore, established that dimensionally modulating single-crystalline olivine-phosphate cathodes ($LiMPO_4$) combined with multi-walled carbon nanotube conductive networks shortcuts solid-state diffusion paths, enabling superior rate capability and structural durability [57]. The mesoporous ZTC additive plays a functionally equivalent role in our composite by drastically lowering effective electrode tortuosity and shortening sodium diffusion lengths into the micropores of the hard carbon host.

To rationalize the kinetic advantages of the target HEZ_ZTC composite electrode, its electrochemical performance can be understood by contrasting the structural traits of zeolite-templated carbon (ZTC) with conventional carbon black (Super P). Commercial Super P consists of non-porous spherical nanoparticles with a low specific surface area [58]. While Super P establishes effective point-to-point electronic conductive pathways across the electrode matrix, it lacks internal porosity; consequently, Na^+ ions are forced to travel

around aggregate clusters through tortuous interparticle voids in the hard carbon host, offering zero ionic flux enhancement. In contrast, ZTC represents a three-dimensional (3D), highly ordered microporous-mesoporous framework featuring uniform mesopores and high conductive structural continuity. In the HEZ_ZTC matrix, ZTC functions as a dual electronic–ionic conductor whose continuous mesopore network acts as liquid electrolyte "fast channels" embedded throughout the active layer. This structural configuration significantly lowers the global electrode tortuosity factor, accelerating liquid-phase ion supply to the microporous HEZ active particles.

To further investigate electrode transport, deconvoluting solid-state bulk diffusion from liquid-phase pore transport is highly valuable, though this analysis introduces notable diagnostic challenges in half-cell configurations. Standard Electrochemical Impedance Spectroscopy (EIS) across 0.01 Hz–100 kHz is frequently complicated by non-stationary behavior stemming from continuous SEI evolution and sodium counter-electrode polarization, which invalidates classical equivalent-circuit parameterization. To circumvent these limitations, kinetic quantification in this study relies on two complementary, SEI-independent methodologies: GITT analysis, which measures apparent Na^+ diffusion coefficients via transient potential relaxation based on Fick's second law, and multi-scan-rate CV, which uses the linear relationship between peak current and $\sqrt{v}$ (Randles–Sevcik equation) to confirm diffusion-limited kinetics [48,49]. The strong convergence of diffusion coefficients derived from both techniques (Table 2) validates the reliability of the reported values. Nevertheless, advanced non-destructive methodologies such as solid-state ^{23}Na pulsed-field gradient NMR spectroscopy or operando potentiostatic electrochemical impedance spectroscopy represent vital future directions to orthogonally decouple phase-specific transport dynamics.

4. Conclusions

Incorporating 10 wt% zeolite-templated carbon (ZTC) as a functional additive into a hazelnut-shell-derived hard carbon (HEZ) anode significantly enhances Na^+ transport kinetics and high-rate performance without requiring alterations to the native hard carbon synthesis. Structural and porosity characterizations confirm a complementary dual-phase architecture: a microporous HEZ matrix integrated with an ordered, interconnected mesoporous ZTC framework (5.7 nm average mesopore diameter). Electrochemical evaluations demonstrate that the HEZ_ZTC composite achieves a fourfold increase in apparent cathodic ionic diffusion coefficient (from ~3.5×10^{-10} $cm^2 \cdot s^{-1}$ to ~16×10^{-10} $cm^2 \cdot s^{-1}$) and superior rate capability. Notably, the HEZ_ZTC electrode maintains a low-voltage plateau capacity of ~100 $mAh \cdot g^{-1}$ after 50 cycles at 50 $mA \cdot g^{-1}$, compared to only ~30 $mAh \cdot g^{-1}$ for pristine HEZ.

While the elevated specific surface area of ZTC (773 m^2 g^{-1}) reduces the initial Coulombic efficiency to 53%, rapid interfacial passivation restores Coulombic efficiency to >99% by the fourth cycle, offsetting initial capacity loss through substantial high-rate gains. Future studies utilizing operando EIS and ^{23}Na solid-state NMR will provide deeper mechanistic insights into SEI evolution and phase-specific ion migration. Furthermore, optimizing ZTC mass loading (e.g., 5–10 wt%) presents a clear pathway to balance initial Coulombic efficiency with high-rate plateau retention, establishing templated mesoporous additives as a viable, synthesis-agnostic strategy for high-power sodium-ion battery anodes.

Supplementary Materials: The following supporting information can be downloaded at: https://www.mdpi.com/article/10.3390/batteries12100385/s1. Figure S1: Proof of zeolite template removal before and after leaching process; Figure S2: Experimental Raman spectra and five-peak deconvoluted fits; Figure S3: Small-angle X-ray scattering (SAXS) analysis; Figure S4: Electrochemical

performance comparison; Table S1: Deconvolution spectral fitting parameters; Table S2: Apparent sodium-ion diffusion coefficients; Table S3: Rate capability discharge capacity values.

Author Contributions: Conceptualization, S.B., C.P. and L.M.; methodology, S.B., C.P. and L.M.; software, L.M.; validation, S.B., C.P. and L.M.; formal analysis, S.B., C.P. and L.M.; investigation, A.A., G.G., S.G., F.R., E.S. and L.M.; resources, S.B., C.P. and L.M.; data curation, S.B., C.P. and L.M.; writing—original draft preparation, L.M.; writing—review and editing, S.B., C.P., S.G., F.R. and L.M.; visualization, S.B., C.P. and L.M.; supervision, S.B. and C.P.; project administration, S.B. and C.P.; funding acquisition, S.B. and C.P. All authors have read and agreed to the published version of the manuscript.

Funding: This work was financed by the Research Fund for the Italian Electrical System (Ministero dell'Ambiente e della Sicurezza Energetica—MASE) under the Three-Year Research Plan 2025–2027 Decree n. 388 of 6 November 2024 "Approvazione del Piano Triennale 2025–2027 della Ricerca di Sistema elettrico", in compliance with Decree n. 139 of 12 April 2024.

Data Availability Statement: The data presented in this study are included in the article and its Supplementary Materials.

Acknowledgments: During the preparation of this study, the authors used Gemini 3 Flash (Google LLC) for developing and optimizing Python-based (Python Software Foundation, v3.12.0) data-processing routines for XRD, Raman, SAXS, CV, and GITT analysis. The authors have reviewed and edited all outputs and take full responsibility for the content of this publication. We acknowledge project 24GRD09 HyMetBat for support with SAXS analysis. This project received funding from the European Partnership on Metrology, co-financed by the European Union's Horizon Europe Research and Innovation Programme and by the Participating States.

Conflicts of Interest: The authors declare that this study was conducted in the absence of any financial or commercial relationships that might create potential conflicts of interest.

Abbreviations

The following abbreviations are used in this manuscript:

HC	Hard Carbon
HEZ	Hazelnut-derived Hard Carbon
ZTC	Zeolite Templated Carbon
XRD	X-Ray Diffraction
FE-SEM	Field Emission Scanning Electron Microscopy
BET	Brunauer–Emmett–Teller (Surface Area Model)
SAXS	Small-Angle X-ray Scattering
TGA	Thermogravimetric Analysis
CV	Cyclic Voltammetry
GC	Galvanostatic Cycling
RC	Rate Capability
GITT	Galvanostatic Intermittent Titration Technique
SSA	Specific Surface Area
d_{002}	Interplanar Spacing
L_c	Crystallite Stacking Height
L_a	Lateral Grain Size/Graphene Plane Extension
I_D/I_G	D and G band Intensity ratio
D_{app}	Apparent Diffusion Coefficient
ICE	Initial Coulombic Efficiency
SEI	Solid Electrolyte Interphase
SoC	State of Charge
Å	Angstrom 10^{-10} m

References

1. Jefferson, T.E.; Rana, S.; Banerjee, N. Lithium-Ion Batteries: A Review of Materials, Design Advances, Sustainability Challenges, and Future Prospects. *Energy Storage* **2025**, *8*, e70320. [CrossRef]
2. Yao, A.; Benson, S.M.; Chueh, W.C. Critically Assessing Sodium-Ion Technology Roadmaps and Scenarios for Techno-Economic Competitiveness against Lithium-Ion Batteries. *Nat. Energy* **2025**, *10*, 404–416. [CrossRef]
3. Gulyas, P. Beyond Lithium: Evaluating Sodium-Ion Batteries for the Next Generation of Electric Vehicles. *Eng. Proc.* **2025**, *113*, 41. [CrossRef]
4. Yabuuchi, N.; Kubota, K.; Dahbi, M.; Komaba, S. Research Development on Sodium-Ion Batteries. *Chem. Rev.* **2014**, *114*, 11636–11682. [CrossRef] [PubMed]
5. Hasa, I.; Mariyappan, S.; Saurel, D.; Adelhelm, P.; Koposov, A.Y.; Masquelier, C.; Croguennec, L.; Casas-Cabanas, M. Challenges of today for Na-based batteries of the future: From materials to cell metrics. *J. Power Sources* **2021**, *482*, 228872. [CrossRef]
6. Gao, Y.; Zhang, H.; Peng, J.; Li, L.; Xiao, Y.; Liu, Y.; Qiao, Y.; Chou, S. A 30-Year Overview of Sodium-Ion Batteries. *Carbon Energy* **2024**, *6*, e464. [CrossRef]
7. Hwang, J.-Y.; Myung, S.-T.; Sun, Y.-K. Sodium-Ion Batteries: Present and Future. *Chem. Soc. Rev.* **2017**, *46*, 3529–3614. [CrossRef] [PubMed]
8. Dou, X.; Hasa, I.; Saurel, D.; Vaalma, C.; Wu, L.; Buchholz, D.; Bresser, D.; Komaba, S.; Passerini, S. Hard Carbons for Sodium-Ion Batteries: Structure, Analysis, and Electrochemistry. *Mater. Today* **2019**, *23*, 87–104. [CrossRef]
9. Irisarri, E.; Ponrouch, A.; Palacin, M.R. Hard Carbon Negative Electrodes in Sodium-Ion Batteries. *J. Electrochem. Soc.* **2015**, *162*, A2476–A2482. [CrossRef]
10. Yin, T.; Guo, Y.; Huang, X.; Yang, X.; Qin, L.; Ning, T.; Tan, L.; Li, L.; Zou, K. Heteroatom Doping Strategy of Advanced Carbon for Alkali Metal-Ion Capacitors. *Batteries* **2025**, *11*, 69. [CrossRef]
11. Ahn, S.; Lagnoni, M.; Yuan, Y.; Ogarev, A.; Vavrinyuk, E.; Voynov, G.; Barrett, E.; Pelli, A.; Atrashchenko, A.; Platonov, A.; et al. Chemical Origins of a Fast-Charge Performance in Disordered Carbon Anodes. *ACS Appl. Energy Mater.* **2023**, *6*, 8455–8465. [CrossRef]
12. Bhawana, K.; Gautam, M.; Mishra, G.K.; Chakrabarty, N.; Wajhal, S.; Kumar, D.; Dutta, D.P.; Mitra, S. Endorsing Na+ storage mechanism in low tortuosity, high plateau capacity hard carbon towards development of high-performance sodium-ion pouch cells. *Carbon* **2023**, *214*, 118319. [CrossRef]
13. Xu, L.Q.; Feng, B.; Su, Y.; Hu, Q.; Liu, G.; Bai, Y.; Chang, S.; Wang, X.; Rodrigue, D.; Hu, J.; et al. Self-supporting, low-tortuosity hard carbon for superior sodium-ion batteries. *Rare Met.* **2024**, *43*, 6362–6372. [CrossRef]
14. Wu, Y.; Chen, H.; Wang, H.; Liu, J.; He, Q.; Que, L.; Wang, X.; Yu, F.; Meng, J.; Lu, C.; et al. High Coulombic efficiency driven by tortuosity gradient regulation for high-performance biomass carbon energy storage materials. *J. Energy Storage* **2024**, *98*, 113162. [CrossRef]
15. Lu, X.; Lian, G.J.; Parker, J.; Ge, R.; Sadan, M.K.; Smith, R.M.; Cumming, D. Effect of carbon blacks on electrical conduction and conductive binder domain of next-generation lithium-ion batteries. *J. Power Sources* **2024**, *592*, 233916. [CrossRef]
16. Zhang, S.; Zheng, M.; Tang, Y.; Zang, R.; Zhang, X.; Huang, X.; Chen, Y.; Yamauchi, Y.; Kaskel, S.; Pang, H. Understanding Synthesis-Structure-Performance Correlations of Nanoarchitectured Activated Carbons for Electrochemical Applications and Carbon Capture. *Adv. Funct. Mater.* **2022**, *32*, 2204714. [CrossRef]
17. Boujibar, O.; Ghamouss, F.; Ghosh, A.; Achak, O.; Chafik, T. Activated carbon with exceptionally high surface area and tailored nanoporosity obtained from natural anthracite and its use in supercapacitors. *J. Power Sources* **2019**, *436*, 226882. [CrossRef]
18. Cao, Y.-M.; Li, X.; Peng, J.; Chen, B.-S.; Dang, N.; Zhang, J.; Xie, J.-Y.; Zhao, T.-B. Acidic Potassium Permanganate-Induced Hierarchical Pores in Bamboo-Based Hard Carbon for High-Performance Sodium-Ion Batteries. *Langmuir* **2025**, *41*, 9559–9566. [CrossRef] [PubMed]
19. Velez, V.; Ramos-Sánchez, G.; Lopez, B.; Lartundo-Rojas, L.; González, I.; Sierra, L. Synthesis of novel hard mesoporous carbons and their applications as anodes for Li and Na ion batteries. *Carbon* **2019**, *147*, 214–226. [CrossRef]
20. Glatthaar, C.; Wang, M.; Wagner, L.Q.; Breckwoldt, F.; Guo, Z.; Zheng, K.; Kriechbaum, M.; Amenitsch, H.; Titirici, M.-M.; Smarsly, B.M. Lignin-Derived Mesoporous Carbon for Sodium-Ion Batteries: Block Copolymer Soft Templating and Carbon Microstructure Analysis. *Chem. Mater.* **2023**, *35*, 10416–10433. [CrossRef] [PubMed]
21. Nishihara, H.; Kyotani, T. Zeolite-templated carbons—Three-dimensional microporous graphene frameworks. *Chem. Commun.* **2018**, *54*, 5648–5673. [CrossRef] [PubMed]
22. Chi, S.; Kim, C.; Lee, Y.; Choi, M. Diversity in Atomic Structures of Zeolite-Templated Carbons and the Consequences for Macroscopic Properties. *JACS Au* **2024**, *4*, 1489–1499. [CrossRef] [PubMed]
23. Kyotani, T.; Nagai, T.; Inoue, S.; Tomita, A. Formation of new type of porous carbon by carbonization in zeolite nanochannels. *Chem. Mater.* **1997**, *9*, 609e615. [CrossRef]
24. Choi, W.; Bera, R.K.; Han, S.W.; Park, H.; Go, T.W.; Choi, M.; Ryoo, R.; Park, J.Y. Doping effect of zeolite-templated carbon on electrical conductance and supercapacitance properties. *Carbon* **2022**, *193*, 42–50. [CrossRef]

25. Hayat, K.; Bahamon, D.; Vega, L.F.; AlHajaj, A. Exploring the Potential of Hierarchical Zeolite-Templated Carbon Materials for High-Performance Li-O_2 Batteries: Insights from Molecular Simulations. *ACS Appl. Mater. Interfaces* **2023**, *15*, 54432–54445. [CrossRef] [PubMed]
26. Dubey, R.J.-C.; Nu, J.; Piveteau, L.; Kravchyk, K.V.; Rossell, M.D.; Campanini, M.; Erni, R.; Kovalenko, M.V.; Stadie, N.P. Zeolite-Templated Carbon as the Cathode for a High Energy Density Dual-Ion Battery. *ACS Appl. Mater. Interfaces* **2019**, *11*, 17686–17696. [CrossRef] [PubMed]
27. Tan, S.; Jean, J.; Pralong, V.; Moldovan, S.; Guo, H.; Mintova, S. Effect of Particle Size on the Sodium Ions Utilization Efficiency of Zeolite-Templated Carbon as the Anode in a Sodium Ion Battery. *Cryst. Growth Des.* **2023**, *23*, 4065–4073. [CrossRef]
28. Borchardt, L.; Leistenschneider, D.; Haase, J.; Dvoyashkin, M. Revising the Concept of Pore Hierarchy for Ionic Transport in Carbon Materials for Supercapacitors. *Adv. Energy Mater.* **2018**, *8*, 1800892. [CrossRef]
29. Ruiz-Rosas, R.; Valero-Romero, M.J.; Salinas-Torres, D.; Rodríguez-Mirasol, J.; Cordero, T.; Morallón, E.; Cazorla-Amorós, D. Electrochemical Performance of Hierarchical Porous Carbon Materials Obtained from the Infiltration of Lignin into Zeolite Templates. *ChemSusChem* **2014**, *7*, 1458–1467. [CrossRef] [PubMed]
30. Park, H.; Terhorst, S.K.; Bera, R.K.; Ryoo, R. Template Dissolution with NaOH-HCl in the Synthesis of Zeolite-Templated Carbons: Effects on Oxygen Functionalization and Electrical Energy Storage Characteristics. *Carbon* **2019**, *155*, 570–579. [CrossRef]
31. Wang, W.; Xu, Y.; Li, Y.; Sun, Y.; Fielding, A.J.; Iamprasertkun, P.; Yang, J.; Wang, B.; Li, Q.; Wu, M.; et al. Evaluation of the Impact of Conductive Additives on the EPR Spectra of Hard Carbon Anodes. *Small Methods* **2026**, *10*, 2500786. [CrossRef] [PubMed]
32. McCreery Research Group. Available online: https://www.chem.ualberta.ca/ mccreery/ramanmaterials.html (accessed on 1 January 2025).
33. Rondino, F.; Falconieri, M.; Gagliardi, S.; Satta, M.; Piccirillo, S.; Bodo, E. Vibrational Spectra of R and S Methyl Para Tolyl Sulfoxide and Their Racemic Mixture in the Solid-Liquid State and in Water Solution. *Symmetry* **2026**, *18*, 17. [CrossRef]
34. Iwashita, N. X-ray Powder Diffraction. In *Materials Science and Engineering of Carbon*; Inagaki, M., Kang, F., Eds.; Butter-worth-Heinemann: Oxford, UK, 2016; pp. 7–25. [CrossRef]
35. Tuinstra, F.; Koenig, J.L. Raman Spectrum of Graphite. *J. Chem. Phys.* **1970**, *53*, 1126–1130. [CrossRef]
36. Ferrari, A.C.; Robertson, J. Interpretation of Raman Spectra of Disordered and Amorphous Carbon. *Phys. Rev. B* **2000**, *61*, 14095–14107. [CrossRef]
37. Sadezky, A.; Muckenhuber, H.; Grothe, H.; Niessner, R.; Pöschl, U. Raman microspectroscopy of soot and related carbonaceous materials: Spectral analysis and structural information. *Carbon* **2005**, *43*, 1731–1742. [CrossRef]
38. Groen, J.C.; Peffer, L.A.A.; Pérez-Ramírez, J. Pore size determination in modified micro- and mesoporous materials. Pitfalls and limitations in gas adsorption data analysis. *Microporous Mesoporous Mater.* **2003**, *60*, 1–17. [CrossRef]
39. Rouquerol, J.; Llewellyn, P.; Rouquerol, F. Is the BET equation applicable to microporous adsorbents? *Stud. Surf. Sci. Catal.* **2007**, *160*, 49–56. [CrossRef]
40. Eddine, S.N.; Daoudi, H.; Kasbaji, M.; Chari, A.; Alami, J.; Dahbi, M.; El Achaby, M.; Kassab, Z. From Biomass to Energy Storage: A Review on Lignocellulosic Biomass-Derived Hard Carbon Anodes for Sodium-Ion Batteries. *Energy Fuels* **2025**, *39*, 17112–17154. [CrossRef]
41. Greco, G.; Del Giudice, A.; Falconieri, M.; Gagliardi, S.; Rondino, F.; Di Pea, M.; Patriarchi, A.; Xhafa, S.; Adelhelm, P.; Brutti, S. Unraveling Microporosity in Hard Carbons: Insights Into Sustainable Sodium-Ion Battery Materials. *Batter. Supercaps* **2026**, *9*, e70430. [CrossRef]
42. Perret, R.; Ruland, W. X-ray small-angle scattering of non-graphitizable carbons. *J. Appl. Cryst.* **1968**, *1*, 308–313. [CrossRef]
43. Smarsly, B.; Antonietti, M.; Wolff, T. Evaluation of the small-angle x-ray scattering of carbons using parametrization methods. *J. Chem. Phys.* **2002**, *116*, 2618–2627. [CrossRef]
44. Aniskevich, Y.; Yu, J.H.; Kim, J.-Y.; Komaba, S.; Myung, S.-T. Tracking Sodium Cluster Dynamics in Hard Carbon with a Low Specific Surface Area for Sodium-Ion Batteries. *Adv. Energy Mater.* **2024**, *14*, 2304300. [CrossRef]
45. Ould, D.M.C.; Oswald, S.; Smith, H.; O'Keefe, C.A.; Song, T.; Kendrick, E.; Wright, D.S.; Grey, C.P. Properties of NaPF6 electrolytes and effect of electrolyte concentration on performance in sodium-ion batteries. *Chem. Commun.* **2025**, *61*, 8516–8519. [CrossRef] [PubMed]
46. Li, J.; Hao, J.; Yuan, Q.; Wang, R.; Marlton, F.; Wang, T.; Wang, C.; Guo, X.; Wang, G. The effect of salt anion in ether-based electrolyte for electrochemical performance of sodium-ion batteries: A case study of hard carbon. *Carbon Energy* **2024**, *6*, e518. [CrossRef]
47. Gogoi, P.; Ge, X.; Janpandit, M.; Prakash, S.; Kalita, N.; Li, Y.C. Investigations on Electrolyte Additives and Formation Mechanism of the Solid Electrolyte Interphase for Sodium Ion Batteries. *ACS Appl. Mater. Interfaces* **2025**, *17*, 13980–13987. [CrossRef] [PubMed]
48. Zhu, Y.; Gao, T.; Fan, X.; Han, F.; Wang, C. Electrochemical Techniques for Intercalation Electrode Materials in Rechargeable Batteries. *ACS Publ. J. Contrib.* **2017**, *50*, 1022–1031. [CrossRef] [PubMed]

49. Santos, R.S.; Felipe, L.F.Z.; Meloni, G.N. Theory in Practice: Testing the Limits of the Randles–Ševčík Equation. *ACS Electrochem.* **2026**, *2*, 478–485. [CrossRef]
50. Kim, J.; Park, S.; Hwang, S.; Yoon, W.S. Principles and applications of galvanostatic intermittent titration technique for lithium-ion batteries. *J. Electrochem. Sci. Technol.* **2021**, *13*, 19–31. [CrossRef]
51. Al-Aoh, H.A.; Badi, N.; El Wanees, S.A.; Alghamdi, S.A.; Al-Anazi, F.A.R.; Manfo, T.A.; Ignatiev, A. Enhanced Electrical Conductivity and Phenol Adsorption of Activated Carbon Fibers Derived from Palm Fiber Waste for Energy Storage and Environmental Applications. *Int. J. Energy Res.* **2026**, *2026*, 4759912. [CrossRef]
52. Dou, X.; Geng, C.; Buchholz, D.; Passerini, S. Research Update: Hard carbon with closed pores from pectin-free apple pomace waste for Na-ion batteries. *APL Mater.* **2018**, *6*, 047501. [CrossRef]
53. Nieto, N.; Porte, J.; Saurel, D.; Djuandhi, L.; Sharma, N.; Lopez-Urionabarrenechea, A.; Palomares, V.; Rojo, T. Use of Hydrothermal Carbonization to Improve the Performance of Biowaste-Derived Hard Carbons in Sodium Ion-Batteries. *ChemSusChem* **2023**, *16*, e202301053. [CrossRef] [PubMed]
54. Wang, Q.; Du, L.; Wang, S.; Yu, L.; Tu, X.; Zhang, H. Biomass-Derived Hard Carbon Anodes Processed with Deep Eutectic Solvents for High-Performance Sodium-Ion Batteries. *ACS Omega* **2025**, *10*, 23620–23628. [CrossRef] [PubMed]
55. Ficca, V.C.A.; Del Giudice, A.; Di Pea, M.; Duranti, L.; Mesina, L.; Placidi, E.; Dell, A.; Brutti, S.; Paoletti, C.; Appetecchi, G.B.; et al. Closing the Loop: Italian Waste Biomass as a Sustainable Source for Sodium-Ion Battery Anodes. *Phys. Status Solidi A Appl. Mater. Sci.* **2026**, *223*, e202500922. [CrossRef]
56. Azemtsop, M.T.; Mehra, R.M.; Kumar, Y.; Gupta, M. Physical Characterization of Ionic Liquid-Modified Polyvinyl Alcohol and Sodium Thiocyanate Polymer Electrolytes for Electrochemical Double-Layer Capacitor Application. *J. Shanghai Jiaotong Univ. (Sci.)* **2023**, *28*, 161–171. [CrossRef]
57. Manfo, T.A.; Laaksonen, H. A comparative study of the modified high voltage olivine-phosphate LiMPO4 (M = Fe, Mn, Co, Ni) as promising cathode materials for next-generation rechargeable batteries. *J. Energy Storage* **2026**, *160*, 121797. [CrossRef]
58. Sawhney, M.A.; Baker, J. Mixing, Fast and Slow: Assessing the Efficiency of Electronically Conductive Networks in Hard Carbon Anodes. *Coatings* **2023**, *13*, 689. [CrossRef]

Disclaimer/Publisher's Note: The statements, opinions and data contained in all publications are solely those of the individual author(s) and contributor(s) and not of MDPI and/or the editor(s). MDPI and/or the editor(s) disclaim responsibility for any injury to people or property resulting from any ideas, methods, instructions or products referred to in the content.